Obstruction and Interference in Low-Energy Models for Twisted Bilayer Graphene

Võ Tiến Phong and E. J. Mele*
Department of Physics and Astronomy, University of Pennsylvania, Philadelphia, Pennsylvania 19104, USA

(Received 28 February 2020; accepted 17 August 2020; published 22 October 2020)

The electronic bands of twisted bilayer graphene (TBLG) with a large-period moiré superlattice fracture to form narrow Bloch minibands that are spectrally isolated by forbidden energy gaps from remote dispersive bands. When these gaps are sufficiently large, one can study a band-projected Hamiltonian that correctly represents the dynamics within the minibands. This inevitably introduces nontrivial geometrical constraints that arise from the assumed form of the projection. Here we show that this choice has a profound consequence in a low-energy experimentally observable signature that therefore can be used to tightly constrain the analytic form of the appropriate low-energy theory. We find that this can be accomplished by a careful analysis of the electron density produced by backscattering of Bloch waves from an impurity potential localized on the moiré superlattice scale. We provide numerical estimates of the effect that can guide experimental work to clearly discriminate between competing models for the low-energy band structure.

DOI: 10.1103/PhysRevLett.125.176404

Twisted van der Waals heterostructures with large-period moiré superlattices are versatile platforms for exploring narrow band physics, and the role of interactions in ground state selection and its excitations. Famously, in magic-angle graphene with a rotation angle $\sim 1°$, the narrow bands near charge neutrality are tuned to a nearly flat condition, and various fractional band fillings are found to support interaction-driven insulating, superconducting, and magnetic states of matter [1–5]. To study the role of these interactions, it is a practical necessity to develop effective low-energy models that faithfully represent the spectral and topological properties. This is, however, a nontrivial task because the topology of the resulting effective model depends crucially on the choice of symmetries one retains in the low-energy projection. Indeed, in the current literature for twisted bilayer graphene (TBLG), there are broadly three classes of such models that are either representable by a minimal local Wannier basis [6,7], fundamentally non-Wannier representable due to a topological obstruction [8,9], or representable by a Wannier basis only with the addition of auxiliary bands [8,10,11]. In this Letter, we propose an experimentally observable signature, which can be used to distinguish between these incompatible models. Motivated by a recent experimental demonstration that the interference pattern of the backscattering of Bloch waves from an impurity can carry information about the Berry phase [12], we propose to distinguish between these different models by carefully analyzing the dark-field reconstruction of the induced change in the local density of states (LDOS) by the presence of a localized impurity on the moiré scale. We emphasize that since the relevant physics concerns the topology and not the flatness of the low-energy bands, our proposal does not require tuning the system to a specific magic angle. In fact, at larger angles like $\theta \sim 1.5°$–$2°$, where complications such as strong interaction-induced renormalization of the band structure, vanishing of the Dirac velocity at the zone corners, and generation of secondary nodal points are absent, our proposal provides a clean test of the relative chirality of the Dirac cones at charge neutrality. Furthermore, because our proposal relies on analyzing signals generated by a moiré-scale impurity, it should not suffer from inevitable noise due to atomic impurities and twist-angle inhomogeneities since these presumably produce much weaker perturbations to the LDOS. For these reasons and others outlined below, the current proposal should be readily achievable in experiments. We note in passing that the method based on wave front interference and dislocation described below is sufficiently generic that it can be adapted to study other Fermi-surface properties of different van der Waals heterostructures [13].

In small-angle TBLG, the low-energy band structure is dominated by strong hybridization of the monolayer Dirac cones induced by interlayer coherence [7,14–18]. The interlayer hopping is conventionally modeled as a smooth local matrix-valued potential acting on the layer and sublattice degrees of freedom that interpolates between the AA and AB/BA registries [14,16–18]. In such a *continuum* theory, microscopic symmetries of the lattice are neglected in favor of emergent symmetries that are approximately preserved at long wavelengths [8–10,19]. Additionally, because the two microscopic valleys are usually well separated in momentum space as shown in Fig. 1(b), a continuum theory typically assumes they are not mixed, introducing a $U_v(1)$ valley symmetry when the

Hamiltonian is decoupled into two independent valley sectors that are related by time-reversal T symmetry. In a single valley, the projected Hamiltonian breaks T symmetry, but retains composite $C_{2z}T$ symmetry and D_3 point symmetries. While none of these symmetries are generally exact, one expects them to be good approximations as long as the relevant physics is insensitive to microscopic details. Valley projection symmetry is of particular importance in our analysis, and will be assumed throughout [6].

Diagonalizing the (spinless) continuum Hamiltonian leads to two weakly dispersive energy bands per valley near charge neutrality that are spectrally isolated from the rest of the band structure. Much work has been devoted to characterizing their topology in hope of identifying a compact effective low-energy description that includes only two orbitals per valley [7–11,20]. This turns out to be a delicate task. If one were to enforce the emergent symmetries of the continuum model, then two Dirac cones form within a single valley with the same chirality. By having opposite mirror eigenvalues for the two bands at an $\bar{M}$ point, the Hamiltonian written in a two-component chiral representation near $\bar{K}$ and $\bar{K}'$ is forced by M_y symmetry to have the same phase winding [8,9], as illustrated in Fig. 1(c). This observation prevents the construction of a local two-orbital tight-binding model defined on a honeycomb lattice which would require two Dirac cones in a single valley with opposite chirality.

Alternatively, one might neglect the emergent symmetries altogether and argue that a generic sample of TBLG usually has no exact M_y symmetry because the twist center that determines the microscopic point symmetries is never under control experimentally. Then, one can posit exponentially localized Wannier orbitals centered at the AB and BA regions. In this case, the resulting tight-binding model constructed from these Wannier orbitals will indeed carry opposite chirality, as illustrated in Fig. 1(d). This approach is appealing because it yields a simple two-orbital model that serves as the starting point for many studies investigating electron interactions in TBLG [21–26]. However, it comes at the cost of relieving the C_2T symmetry protection of the linear band crossings.

Recently, it has been proposed and experimentally demonstrated that Friedel oscillations of LDOS due to backscattering from a localized impurity not only carry spectral information but also encode Berry-phase information [12,27], which renders them a crucial diagnostic tool for examining momentum-space topology. As this is the distinguishing feature between the different low energy models outlined above, here we adapt this insight to study Friedel oscillations in TBLG to probe the subtler issue of the assignment of chiral structure to its narrow bands.

First, we consider a valley-polarized two-orbital model that describes the low-energy spectrum of TBLG. This model is formally equivalent to the model of monolayer graphene, and as such, it can be represented using two

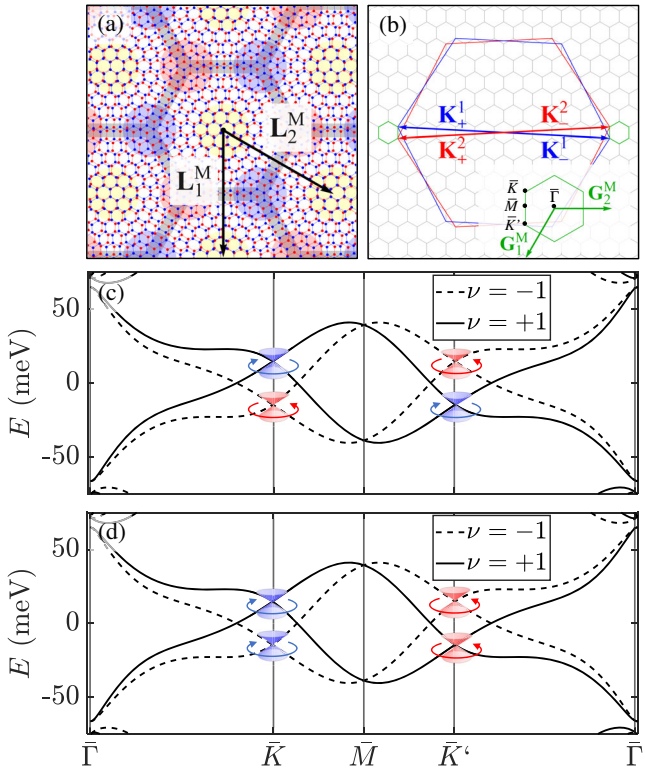

FIG. 1. (a) Honeycomb moiré lattice structure of TBLG, spanned by $\mathbf{L}_1^M$ and $\mathbf{L}_2^M$, is formed by starting with an AA-stacked bilayer system and then twisting one layer relative to the other by an angle θ. The resulting structure is a long-wavelength moiré pattern that has AA regions (yellow-shaded), AB regions (red-shaded), and BA regions (blue-shaded). (b) Mini-Brillouin zone (MBZ) of TBLG formed by the momentum-mismatch of the original Brillouin zones. The blue and red hexagons show the monolayer BZs rotating in opposite directions. The MBZ is shown in green with high-symmetry points $\bar{K}$, $\bar{K}'$, $\bar{M}$, and $\bar{\Gamma}$, and reciprocal lattice vectors $\mathbf{G}_1^M$ and $\mathbf{G}_2^M$. (c)–(d) Band structure of TBLG numerically calculated from the continuum model with $\theta = 2°$, $w_{AA} = 79.7$ meV, $w_{AB} = 97.5$ meV, and $\hbar v_F/a = 2135.4$ meV. We also apply an interlayer bias $V = 200$ meV to shift the Dirac cones to improve visibility. The dash and solid lines are energy bands for the $-$ and $+$ valleys, respectively. We observe two Dirac cones in each valley at $\bar{K}$ and $\bar{K}'$. We indicate the chirality of the band crossings schematically by blue and red cones. Dirac cones in the same valley have the same chirality in (c), corresponding to the topology of the continuum model, and opposite chirality in (d), corresponding to the topology of a two-orbital tight-binding model.

exponentially localized Wannier orbitals per valley centered at the AB and BA regions. In the Bloch basis, the Hamiltonian expanded to linear order in momentum around the zone corners is

$$\mathcal{H}(\bar{\mathbf{K}} + \mathbf{q}) = -\hbar\tilde{v}_F \mathbf{q}\cdot\boldsymbol{\sigma}^*,$$
$$\mathcal{H}(\bar{\mathbf{K}}' + \mathbf{q}) = -\hbar\tilde{v}_F \mathbf{q}\cdot\boldsymbol{\sigma}, \quad (1)$$

where $\boldsymbol{\sigma} = (\sigma_x, \sigma_y)$ are Pauli matrices, $\tilde{v}_F$ is the renormalized velocity that depends on interlayer hopping

amplitudes, w_{AA} and w_{AB}, and $\mathbf{q}$ is measured from the respective zone corners. Written in the chiral representation, $\mathcal{H}(\mathbf{k}) = \mathbf{d}(\mathbf{k}) \cdot \boldsymbol{\sigma}$ for some vector-valued function $\mathbf{d}(\mathbf{k})$, the chirality of some twofold degenerate point $\mathbf{k}_c$ is defined as the integer winding number of $\mathbf{d}(\mathbf{k})$ as $\mathbf{k}$ goes around counterclockwise any simple closed loop that contains $\mathbf{k}_c$. In Eq. (1), $\mathbf{d}(\mathbf{q}) = (q_x, -q_y)$ near $\bar{\mathbf{K}}$ and $\mathbf{d}(\mathbf{q}) = (q_x, q_y)$ near $\bar{\mathbf{K}}'$, which shows that the Dirac cones carry opposite chirality in this model. For Bloch wave functions with wave vectors near a Dirac cone, the chirality defines the relative phase between the two sublattices. This phase difference will be crucial in the consideration of scattering processes induced by the presence of an impurity, especially in the detection of the relative chirality between two Dirac cones.

We now place a spatially localized impurity atop one of the Wannier orbitals, as shown schematically in Fig. 2(a). Suppose this impurity contains a resonant bound state with energy U_0 that has significant wave function overlap with only the Wannier orbital on which it sits, say the AB orbital, then the scattering potential in the basis of Eq. (1) simplifies to

$$\mathcal{U}(\mathbf{r}, \mathbf{r}') \approx U_0 \begin{pmatrix} 1 & 0 \\ 0 & 0 \end{pmatrix} \delta^{(2)}(\mathbf{r}) \delta^{(2)}(\mathbf{r}'). \tag{2}$$

Using this approximation, we can calculate the induced change in LDOS using the Green's function formalism. This framework is especially convenient when the impurity can be modeled as an delta impurity in the Wannier basis as in Eq. (2). We should emphasize that Eq. (2) holds for an impurity localized on the moiré scale, not the atomic scale.

The change in LDOS at energy E is given by $\Delta\rho(E, \mathbf{r}) = -\pi^{-1} \Im \mathrm{Tr}[\mathcal{G}^{(0)}(E, \mathbf{r}) \mathcal{T}(E) \mathcal{G}^{(0)}(E, -\mathbf{r})]$, where $\mathcal{G}^{(0)}(E, \mathbf{r})$ is the bare Green's function, and $\mathbf{r}$ is measured from the location of the impurity. The trace is taken over the Wannier sublattice degree of freedom. When E is sufficiently close to the energy of the Dirac cones, we use Eq. (1) to calculate the bare Green's function exactly [28]. We find that the momentum-space phase in the Hamiltonian that defines the chirality is mapped to a real-space phase in the bare Green's function upon integration over all momenta near the Dirac cones [12]. For scattering processes that exchange momentum within the same Dirac cone, this real-space phase cancels out, but for scattering processes that exchange momentum between different Dirac cones within a single valley, this real-space phase instead has a nontrivial signature for the interference pattern of LDOS. Explicitly, we decompose $\Delta\rho(E, \mathbf{r})$ into two parts

$$\begin{aligned} \Delta\rho(E, \mathbf{r}) &= \Delta\rho_{\mathrm{intra}}(E, \mathbf{r}) + \Delta\rho_{\mathrm{inter}}(E, \mathbf{r}), \\ \Delta\rho_{\mathrm{intra}}(E, \mathbf{r}) &\propto \Im\{t(E)[K_0^2(r/i\ell) - K_1^2(r/i\ell)]\}, \\ \Delta\rho_{\mathrm{inter}}(E, \mathbf{r}) &\propto \Im[t(E) K_1^2(r/i\ell)] \cos(\Delta\bar{\mathbf{K}} \cdot \mathbf{r} - 2\phi_{\mathbf{r}}) \\ &\quad - \Im[t(E) K_0^2(r/i\ell)] \cos(\Delta\bar{\mathbf{K}} \cdot \mathbf{r}), \end{aligned} \tag{3}$$

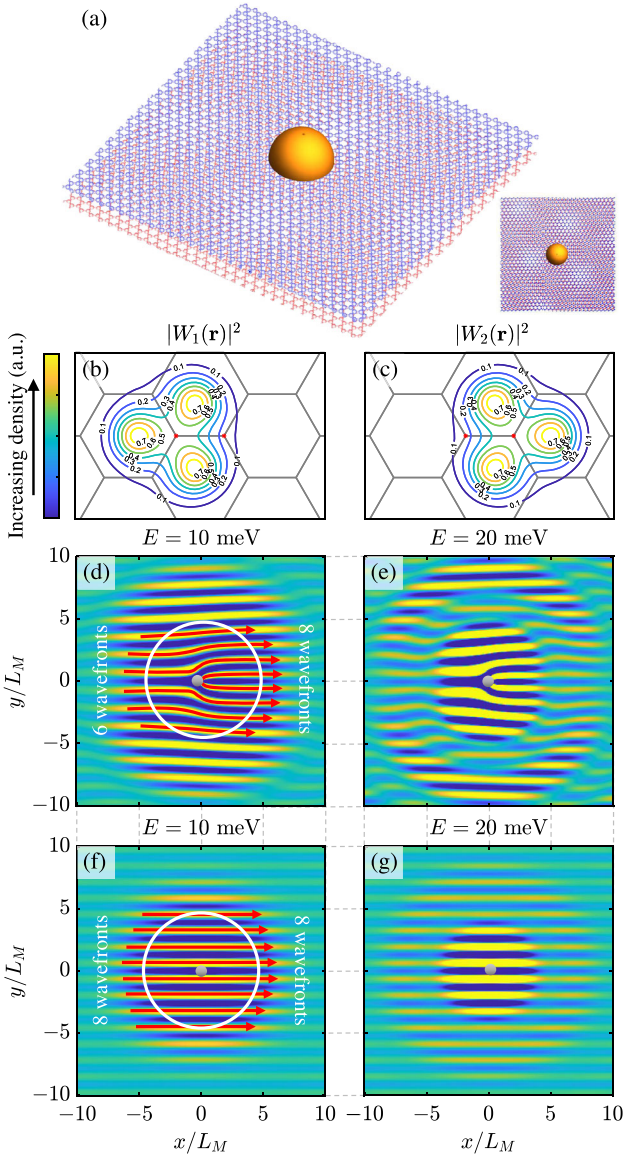

FIG. 2. (a) Schematic representation of a possible experimental setup in which an impurity is placed atop an AB region. (b),(c) The spatial distribution of the two Wannier orbitals in a single valley of TBLG. $|W_1\rangle$ and $|W_2\rangle$ are centered at an AB and BA region, respectively; however, most of their density is concentrated at the adjacent AA regions. (d),(e) The LDOS simulated from inter-Dirac-cone scatterings at a bias energy $E = 10$ meV and $E = 20$ meV for the Wannier-representable model where the chirality at the two Dirac cones is opposite. We observe two wave front dislocations in the interference pattern. In addition, we also observe that as the probing energy increases, the period of radial oscillations decreases. (f),(g) The LDOS simulated from inter-Dirac-cone scatterings for the Wannier-obstructed model where the chirality at the two Dirac cones is opposite. Unlike before, here, we observe no wave front dislocations.

where $\Delta\bar{\mathbf{K}} = \bar{\mathbf{K}} - \bar{\mathbf{K}}'$, $\ell = \hbar\tilde{v}_F/E$, $t(E)$ is the nonzero matrix element of $\mathcal{T}(E)$, $\phi_{\mathbf{r}}$ is the real-space angle, and $K_\alpha(z)$ is the αth modified Bessel function of the second kind. From Eq. (3), we observe that $\Delta\rho_{\mathrm{intra}}(E, \mathbf{r})$ is only a

function of the radial direction. $\Delta\rho_{\text{inter}}(E,\mathbf{r})$ is more interesting; in addition to radial oscillations with period ℓ coming from the Bessel functions, there are also wave fronts propagating in the $\Delta\bar{\mathbf{K}}$ direction with period $|\Delta\bar{\mathbf{K}}|^{-1}$. Importantly, the two oscillatory terms differ by a spatial phase $2\phi_{\mathbf{r}}$. To understand the effect of this phase, we write $\cos(\Delta\bar{\mathbf{K}}\cdot\mathbf{r}-2\phi_{\mathbf{r}})=\cos(\Delta\bar{\mathbf{K}}\cdot\mathbf{r})\cos(2\phi_{\mathbf{r}})+\sin(\Delta\bar{\mathbf{K}}\cdot\mathbf{r})\sin(2\phi_{\mathbf{r}})$, and observe that the wave fronts are modulated by trigonometric functions that change signs *twice* as we go around a simple closed loop, resulting in two wave front dislocations. If we go around in a circle at a fixed r for which $\Im[t(E)K_0^2(r/i\ell)]<\Im[t(E)K_1^2(r/i\ell)]$, then the change in LDOS contains these two wave front dislocations, as shown in Figs. 2(d) and 2(e). The prefactor of $\phi_{\mathbf{r}}$ is given by the difference in chirality of the two Dirac cones, and thus the presence of wave front dislocations in LDOS is a measure of the relative chirality. The LDOS obtained experimentally will contain all backscattering processes, including those related by reciprocal lattice vectors. Because of that, to observe the density dislocations in practice, we need to filter out only time-reversed pairs of momenta that are near the relevant Dirac cones, as illustrated in Fig. 3. Then, the dislocations, if present, will be contained in the dark-field reconstruction of the LDOS.

We now consider a different effective model of TBLG in which the flat-band Dirac cones in the same valley have identical chirality. In this case, it is not possible to construct a tight-binding model which contains only two orbitals and still retains a local representation of the C_2T symmetry that protects the valley-projected Dirac points. We need to include additional bands to capture the correct topology, as done in [8]. However, these auxiliary bands can be sent to high energies since they do not correspond to the actual band structure of TBLG. Thus, as long as we are probing at energies close to the Dirac cones, these auxiliary bands can be safely neglected. In this limit, the low-energy effective Hamiltonian is similar to Eq. (1), but the chirality is identical at the two cones

$$\mathcal{H}(\bar{\mathbf{K}}+\mathbf{q})=-\hbar\tilde{v}_F\mathbf{q}\cdot\boldsymbol{\sigma},$$
$$\mathcal{H}(\bar{\mathbf{K}}'+\mathbf{q})=-\hbar\tilde{v}_F\mathbf{q}\cdot\boldsymbol{\sigma}. \tag{4}$$

If we now place an impurity in this system with scattering potential as in Eq. (2), then the induced change in LDOS will not feature wave front dislocations previously seen, as shown in Figs. 2(f) and 2(g). This markedly different interference pattern serves as a diagnostic of the two competing effective models of the valley-projected flat bands in TBLG.

To illustrate the analysis procedure from experimental data, we study impurities localized on the atomic scale located at $\mathbf{s}$ within a moiré unit cell calculated directly from the continuum model [28,29]. The presence of a dislocation in LDOS depends on $\mathbf{s}$, and appears only in the fast-Fourier-transform-filtered images. When $\mathbf{s}$ is in the *AA* region, we do not observe a dislocation, but when $\mathbf{s}$ is in a region where the sublattice on which the impurity sits is aligned with another sublattice of the other layer, then we observe one wave front dislocation, shown in Fig. 3. Even though atomic impurities serve as illustration of nontrivial density dislocations, they are not practically relevant since their signals are difficult to disentangle from those of disorder.

Our analysis so far relies crucially on the ability to design an impurity that polarizes one Wannier sublattice. This is, however, a nontrivial task because the Wannier orbitals in TBLG are spatially distributed and overlapping [6–8], as shown in Figs. 2(b) and 2(c). It is known that the Wannier

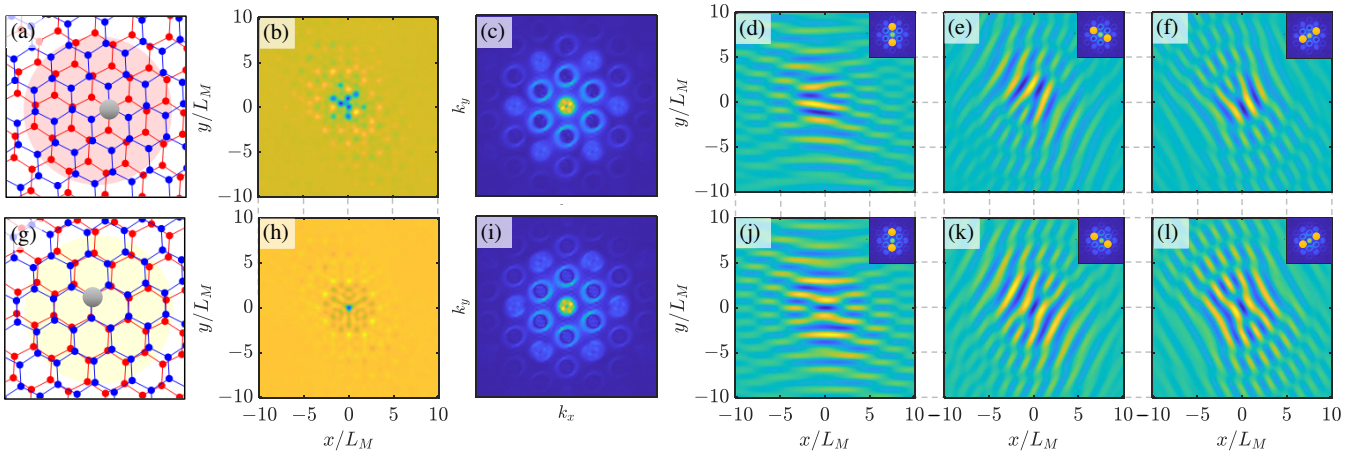

FIG. 3. Each row shows the change in LDOS induced by an impurity placed on an *AB* region (top row) or an *AA* region (bottom row). (b) and (h) show the full interference pattern, and (c) and (i) show the magnitudes of their fast Fourier transforms (FFT). From the FFT, we filter out time-reversed pairs of momenta in three independent directions, and then calculate the inverse FFT to observe the density wave fronts. Panels (d)–(f) and (j)–(i) show the wave front interference pattern after applying corresponding FFT filters indicated on the insets. As can clearly be seen, (d)–(f) feature one wave front dislocation. On the contrary, (j)–(l) do not have any dislocation.

orbitals in a single valley have $p_\pm$ symmetry [7,8]. So if the resonant bound state carries angular momentum $m \neq \pm 1$, then its overlap with the Wannier orbital on which it is centered vanishes. In particular, if we place a T-symmetric quantum dot centered on an AB region, then its bound state will only have significant overlap with Wannier orbitals at the three neighboring BA regions. In this case, the far-field interference patterns induced will be identical to those produced by the scattering potential in Eq. (2). This establishes the relevance of our proposal in experimental settings. Next, we provide some parameter estimates as further motivation, using values from [7]. In a scanning tunneling spectroscopy (STS) experiment that probes LDOS, the bias potential must be set at an energy where the linear approximation to the flat bands holds. Approaching the magic angle, this is challenging because the bandwidth there becomes quite small. At slightly larger angles, $\theta = 2°$–$1.5°$, the bias potential can be several tens of meV, well within experimental capacity. The period of the wavefronts is $|a\Delta\tilde{\mathbf{K}}|^{-1} \approx 6$–$8$, while the decay of the radial oscillation is $\ell E/a = 500$–1000 meV for $\theta = 2°$–$1.5°$. In order to clearly observe the density dislocations, we must probe at an energy low enough where $\ell > |\Delta\tilde{\mathbf{K}}|^{-1}$. However, it must not be too small that the amplitude of LDOS is suppressed, $V_{\text{cell}}\Delta\rho \sim U_0 E^2/(10^6\ \text{meV}^4)$ for $\theta = 2°$–$1.5°$, where V_{cell} is the unit-cell area and U_0 is small. The scanning window must span multiple wave fronts in order to observe the dislocations, on the order of 100–200 graphene lattice constants.

We emphasize that this proposal for experimentally defining the topology of the low-energy bands needs not be restricted to the magic-angle regime. In fact, there are some distinct advantages, both in principle and in practice, to studying larger nearby angles where the low-energy bands are predicted to be more dispersive, and the zone corners can be well approximated by massless Dirac dispersions. The bandwidth at these larger angles is greatly enhanced, making the active bands easier to interrogate by varying the tip potentials. Furthermore, for larger angles, the moiré period becomes shorter, making it easier to scan many periods with STS. Mixing between valleys can occur at larger angles, but for $\theta \sim 1.5°$–$2.0°$, where the two valleys are still well-separated in momentum space, we expect this effect to remain minimal. For angles very close to a magic angle, it will be important to extend this approach to look at the effects of mean-field interaction-driven density wave instabilities.

We thank Francisco Guinea, Abhay Pasupathy, and Oskar Vafek for fruitful conversations. V. T. P. acknowledges financial support from the National Science Foundation through the Graduate Research Fellowship Program and from the P. D. Soros Fellowship for New Americans. E. J. M.'s work on this problem is supported by the Department of Energy under Grant No. DE-FG02-84ER45118.

*mele@physics.upenn.edu

[1] Y. Cao, V. Fatemi, S. Fang, K. Watanabe, T. Taniguchi, E. Kaxiras, and P. Jarillo-Herrero, Nature (London) **556**, 43 (2018).
[2] Y. Cao, V. Fatemi, A. Demir, S. Fang, S. L. Tomarken, J. Y. Luo, J. D. Sanchez-Yamagishi, K. Watanabe, T. Taniguchi, E. Kaxiras *et al.*, Nature (London) **556**, 80 (2018).
[3] M. Yankowitz, S. Chen, H. Polshyn, Y. Zhang, K. Watanabe, T. Taniguchi, D. Graf, A. F. Young, and C. R. Dean, Science **363**, 1059 (2019).
[4] X. Lu, P. Stepanov, W. Yang, M. Xie, M. A. Aamir, I. Das, C. Urgell, K. Watanabe, T. Taniguchi, G. Zhang *et al.*, Nature (London) **574**, 653 (2019).
[5] A. L. Sharpe, E. J. Fox, A. W. Barnard, J. Finney, K. Watanabe, T. Taniguchi, M. A. Kastner, and D. Goldhaber-Gordon, Science **365**, 605 (2019).
[6] J. Kang and O. Vafek, Phys. Rev. X **8**, 031088 (2018).
[7] M. Koshino, N. F. Q. Yuan, T. Koretsune, M. Ochi, K. Kuroki, and L. Fu, Phys. Rev. X **8**, 031087 (2018).
[8] L. Zou, H. C. Po, A. Vishwanath, and T. Senthil, Phys. Rev. B **98**, 085435 (2018).
[9] H. C. Po, L. Zou, A. Vishwanath, and T. Senthil, Phys. Rev. X **8**, 031089 (2018).
[10] Z. Song, Z. Wang, W. Shi, G. Li, C. Fang, and B. A. Bernevig, Phys. Rev. Lett. **123**, 036401 (2019).
[11] J. Ahn, S. Park, and B.-J. Yang, Phys. Rev. X **9**, 021013 (2019).
[12] C. Dutreix, H. González-Herrero, I. Brihuega, M. I. Katsnelson, C. Chapelier, and V. T. Renard, Nature (London) **574**, 219 (2019).
[13] V. O. Özçelik, J. G. Azadani, C. Yang, S. J. Koester, and T. Low, Phys. Rev. B **94**, 035125 (2016).
[14] J. M. B. Lopes dos Santos, N. M. R. Peres, and A. H. Castro Neto, Phys. Rev. Lett. **99**, 256802 (2007).
[15] E. Suárez Morell, J. D. Correa, P. Vargas, M. Pacheco, and Z. Barticevic, Phys. Rev. B **82**, 121407(R) (2010).
[16] E. J. Mele, Phys. Rev. B **81**, 161405(R) (2010).
[17] R. Bistritzer and A. H. MacDonald, Proc. Natl. Acad. Sci. U.S.A. **108**, 12233 (2011).
[18] F. Guinea and N. R. Walet, Phys. Rev. B **99**, 205134 (2019).
[19] M. Angeli, D. Mandelli, A. Valli, A. Amaricci, M. Capone, E. Tosatti, and M. Fabrizio, Phys. Rev. B **98**, 235137 (2018).
[20] H. C. Po, L. Zou, T. Senthil, and A. Vishwanath, Phys. Rev. B **99**, 195455 (2019).
[21] M. Fidrysiak, M. Zegrodnik, and J. Spałek, Phys. Rev. B **98**, 085436 (2018).
[22] J. W. F. Venderbos and R. M. Fernandes, Phys. Rev. B **98**, 245103 (2018).
[23] Y.-P. Lin and R. M. Nandkishore, Phys. Rev. B **98**, 214521 (2018).
[24] A. Thomson, S. Chatterjee, S. Sachdev, and M. S. Scheurer, Phys. Rev. B **98**, 075109 (2018).
[25] Z. Zhu, D. N. Sheng, and L. Fu, Phys. Rev. Lett. **123**, 087602 (2019).
[26] Y. Da Liao, Z. Y. Meng, and X. Y. Xu, Phys. Rev. Lett. **123**, 157601 (2019).
[27] C. Dutreix and P. Delplace, Phys. Rev. B **96**, 195207 (2017).
[28] See the Supplemental Material at http://link.aps.org/supplemental/10.1103/PhysRevLett.125.176404 for a

discussion of the continuum model and the Green's function method, and it contains Refs. [7–9,14,16–18,29–45].
[29] K. Seki and S. Yunoki, Phys. Rev. B **93**, 245115 (2016).
[30] J. M. B. Lopes dos Santos, N. M. R. Peres, and A. H. Castro Neto, Phys. Rev. B **86**, 155449 (2012).
[31] N. N. T. Nam and M. Koshino, Phys. Rev. B **96**, 075311 (2017).
[32] M. Koshino and N. N. T. Nam, Phys. Rev. B **101**, 195425 (2020).
[33] P. Lucignano, D. Alfè, V. Cataudella, D. Ninno, and G. Cantele, Phys. Rev. B **99**, 195419 (2019).
[34] L. A. Gonzalez-Arraga, J. L. Lado, F. Guinea, and P. San-Jose, Phys. Rev. Lett. **119**, 107201 (2017).
[35] E. N. Economou, *Green's Functions in Quantum Physics*, Vol. 7 (Springer Science & Business Media, New York, 2006).
[36] M. I. Katsnelson, *Graphene: Carbon in Two Dimensions* (Cambridge University Press, Cambridge, England, 2012).
[37] D. Vanderbilt, *Berry Phases in Electronic Structure Theory: Electric Polarization, Orbital Magnetization and Topological Insulators* (Cambridge University Press, Cambridge, England, 2018).
[38] J. Rath and A. J. Freeman, Phys. Rev. B **11**, 2109 (1975).
[39] P. E. Blöchl, O. Jepsen, and O. K. Andersen, Phys. Rev. B **49**, 16223 (1994).
[40] C. Dutreix, H. González-Herrero, I. Brihuega, M. I. Katsnelson, C. Chapelier, and V. T. Renard, Nature (London) **574**, 219 (2019).
[41] K. Hejazi, C. Liu, H. Shapourian, X. Chen, and L. Balents, Phys. Rev. B **99**, 035111 (2019).
[42] P. San-Jose and E. Prada, Phys. Rev. B **88**, 121408(R) (2013).
[43] D. K. Efimkin and A. H. MacDonald, Phys. Rev. B **98**, 035404 (2018).
[44] B. Tsim, N. N. T. Nam, and M. Koshino, Phys. Rev. B **101**, 125409 (2020).
[45] G. Tarnopolsky, A. J. Kruchkov, and A. Vishwanath, Phys. Rev. Lett. **122**, 106405 (2019).